Journal of Optics

PURPOSE-LED PUBLISHING™

ACCEPTED MANUSCRIPT

A broadband polarization splitting device with sub-micron sized pixels

To cite this article before publication: Farhan Ali *et al* 2025 *J. Opt.* in press https://doi.org/10.1088/2040-8986/adda5c

Manuscript version: Accepted Manuscript

Accepted Manuscript is "the version of the article accepted for publication including all changes made as a result of the peer review process, and which may also include the addition to the article by IOP Publishing of a header, an article ID, a cover sheet and/or an 'Accepted Manuscript' watermark, but excluding any other editing, typesetting or other changes made by IOP Publishing and/or its licensors"

This Accepted Manuscript is **© 2025 IOP Publishing Ltd. All rights, including for text and data mining, AI training, and similar technologies, are reserved.**.

During the embargo period (the 12 month period from the publication of the Version of Record of this article), the Accepted Manuscript is fully protected by copyright and cannot be reused or reposted elsewhere.

As the Version of Record of this article is going to be / has been published on a subscription basis, this Accepted Manuscript will be available for reuse under a CC BY-NC-ND 4.0 licence after the 12 month embargo period.

After the embargo period, everyone is permitted to use copy and redistribute this article for non-commercial purposes only, provided that they adhere to all the terms of the licence https://creativecommons.org/licences/by-nc-nd/4.0

Although reasonable endeavours have been taken to obtain all necessary permissions from third parties to include their copyrighted content within this article, their full citation and copyright line may not be present in this Accepted Manuscript version. Before using any content from this article, please refer to the Version of Record on IOPscience once published for full citation and copyright details, as permissions may be required. All third party content is fully copyright protected, unless specifically stated otherwise in the figure caption in the Version of Record.

View the article online for updates and enhancements.

This content was downloaded from IP address 146.103.254.11 on 20/05/2025 at 12:38

A broadband polarization splitting device with sub-micron sized pixels

F. Ali[1,2], B. Figeys[1], O. Shramkova[1], R. M. Ciarnain[1], X. Rottenberg[1,3], R. Gehlhaar[1] and J. Genoe[1,2]

[1]Imec, Kapeldreef 75, 3001 Leuven, Belgium, email: farhan.ali@imec.be
[2]KU Leuven, ESAT department, Kasteelpark Arenberg 10 - bus 2440, 3001 Leuven, Belgium
[3]ULB, Ecole Polytechnique de Bruxelles, Av. Franklin Roosevelt 50 1050 Brussels, Belgium

Abstract

Integration of polarization sensing into conventional imaging devices can uncover crucial information, unlocking applications across a wide range of scientific domains from biomedical imaging to remote sensing and astronomy. Rapid progress in nanofabrication technology has driven the trend of pixel downscaling in imaging devices, leading to improved device functionality and performance. For polarization imaging to engage with high-resolution image sensor a further scaling of per-pixel polarizing objects is needed, while maintaining the optical throughput. In this paper, we propose a design for an ultracompact polarization splitting device based on a vertical dielectric waveguide architecture, compatible with sub-micron pixel sizes (560 nm), which is close to the state-of-the-art CMOS imager sensor resolution. The device implements an adiabatic mode converter to effectively separate orthogonal linear polarization states of incident light across the entire visible spectrum. Moreover, we demonstrate the design versatility by expanding its polarization splitting functionality across the entire linear polarization space (0º-180º), enabling robust polarization detection for advanced polarization imaging applications.

Keywords: Polarization splitting, Ultracompact polarization splitter, Vertical waveguides, Polarization imaging, high-resolution imagers

Introduction

The polarization of light contains useful information to reveal features like shape, texture and shading of a reflecting surface [1],[2]. From condition-robust surveillance to space exploration and biomedical imaging, polarization of light has widespread implications across numerous science and engineering domains [3]-[8]. Many biological specimens use light's polarization property to perform useful tasks like navigating their environment, object detection and predating [9]-[11]. In contrary, the human eye is only weakly polarization sensitive [12],[13] and most people are incapable of visualizing the polarization of light.

Owing to technological and nanofabrication advancement, polarization image sensors have emerged in the field of polarimetric imaging [14]-[17]. These sensors typically comprise a pixelated polarization filter array on an imaging device [18],[19]. Conventional polarization filters may compose of metallic nanowires, birefringent crystals, or polarizing thin films to filter polarization [20]-[23]. Each pixel in the imaging device

Accepted Manuscript

records light intensity with a different polarization, and is used to quantify the intensity of the respective polarization. Eventually, the polarization state of the incident light can be determined from the respective polarization components. However, a major issue with traditional polarization filters is that they discard a significant portion of the incoming light, limiting the theoretical efficiency to 50% [24]. Hence, there is an incentive to design novel polarimetric imaging devices with higher light sensitivity.

Polarization splitting is a novel approach which offers an alternative to conventional filtering methods. Instead of filtering photons of unwanted polarization states, it separates the incident light beam into its constituent polarization components and re-directs to specific pixels without significant loss. Besides overcoming the 50% efficiency limit set by a polarization filter, splitting devices have the design freedom for much smaller and compact optical systems, thus enabling applications like remote sensing and communication. Recently, optical metasurfaces have achieved polarization splitting functionality as these artificial planar structures can efficiently control the phase, amplitude, and polarization of electromagnetic waves at optical frequencies [25]-[29]. To date, several plasmonic and dielectric based metasurfaces have been reported to perform polarimetry via full Stokes vector measurements [30]-[36]. Notably, Arbabi et al. proposed a high contrast dielectric metasurface to realize polarimetric imaging at NIR frequency with a high transmission efficiency (>60%) at a spatial resolution of 2.4 μm [24]. However, none of the reported metasurfaces have been designed with sub-micron pixel size to integrate them into high-resolution imaging devices. There are yet devices needed to follow the pixel downscaling trend for polarimetric imaging devices [37].

Here, we introduce a novel broadband polarization splitting device based on vertical Silicon Nitride (Si_3N_4) waveguides operating in the visible spectrum (400-700 nm). The demonstrated device employs an adiabatic taper to separate the incident light with orthogonal linear polarization states and route to designated pixels at sub-micron spatial resolution. Our numerical simulations show a transmission efficiency surpassing 95% with a minimal reflection (<5%). In addition, incorporation of half-waveplate elements expands the capability to split polarizations across the complete linear polarization space (0^o-180^o). With its compact footprint, broadband operation, and exceptional transmission efficiency, our proposed polarization splitter has the potential to replace conventional polarization splitting devices, thus paving the way for the development of ultracompact and high-resolution polarization imaging devices.

Design and Simulation of Polarization Splitters

The proposed broadband polarization splitter (PS) is based on a periodic array of vertical waveguides comprising a Silicon Nitride (Si_3N_4) core and a SiO_2 cladding (Fig.1a). A Silicon Oxide (SiO_2) anti-reflection coating (ARC) layer is placed on the top of the waveguide entrances reducing reflections to maximize the device efficiency. Figure 1b shows a unit cell design with pitch P = 0.8 μm, comprised of a vertical waveguide with the corresponding geometrical parameters and cross-sectional views at A, B, and C planes along the propagation direction. The waveguide consists of two segments, the input waveguide and splitting waveguides, with lengths 3.1 μm and 7.2 μm respectively. The top segment has a square-shaped input cross section (plane A) with width 650 nm**,** which tapers down asymmetrically to two partially overlapping orthogonal rectangular waveguides of dimension 650 nm $\times$ 200 nm, forming an L-shaped cross section at plane

Accepted Manuscript

B. The bottom segment consists of two orthogonal superimposed waveguides with an L-shaped cross section, which gradually separates and tapers down to two square-shaped cross sections of width 200 nm (plane C). Figure 1c depicts an arrangement of the pixels in the detector plane, composed of two pixels named as left, right with dimensions 560 nm × 560 nm to capture the orthogonal polarizations of light along x and y.

The basic function of the input waveguide is to adiabatically transmit the input beam to the partially overlapped splitting waveguides at the interface of both segments. The size and geometry of the input waveguide at the entrance plane leads to the existence of two degenerate fundamental modes in the waveguide for the orthogonal polarization states[38]. The designed structure allows excitation of these modes with the electric field aligned along either horizontal (X) or vertical (Y) directions as shown by the red arrows in Figure 1b. As the input beam is adiabatically transferred from the input waveguide to the L-shaped cross section at plane B, the beam is guided to either of the splitting waveguides with the electric field aligned along the long axis of the waveguide. The guided beam is further guided towards the square-shaped waveguides and separates from its counterpart waveguide at plane C, minimizing the intensity cross-talk. Finally, the input beam ends up in either of the left/right pixels depending on its polarization state.

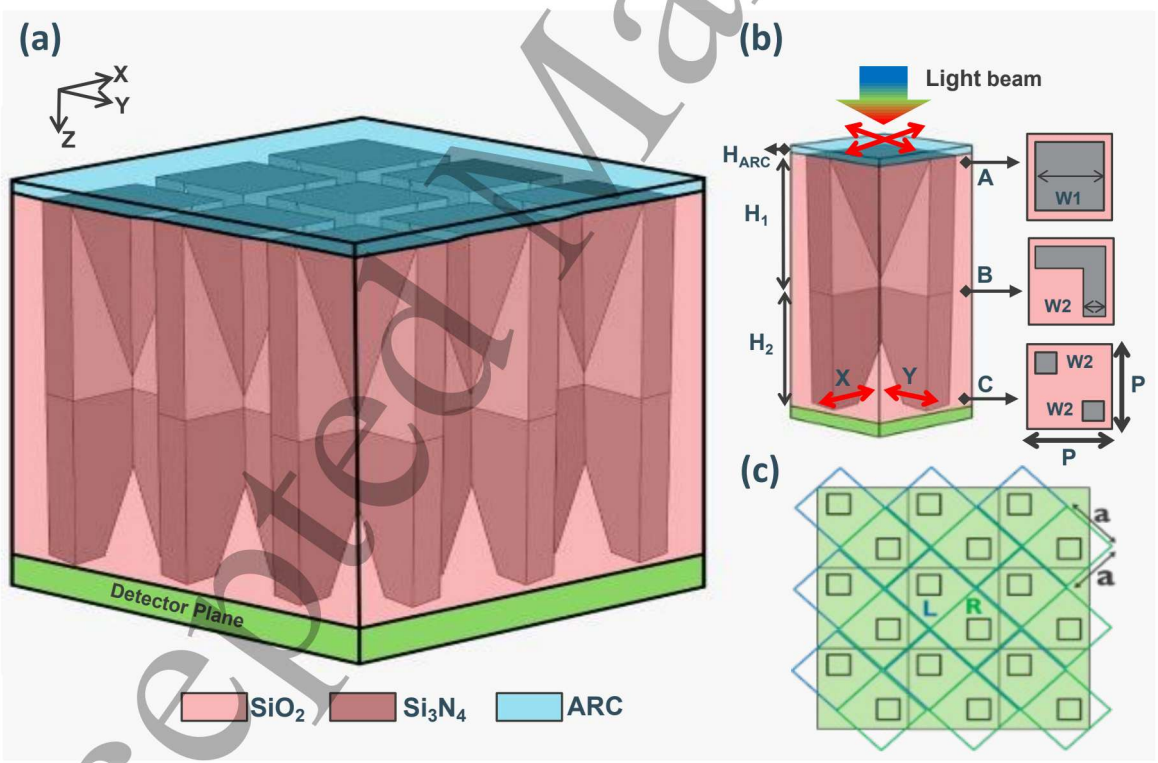

Figure 1. Design of a broadband polarization splitter based on Silicon Nitride vertical waveguides. (a) A Schematics of Si_3N_4 polarization splitters array embedded in SiO_2 matrix, with an anti-reflection coating (ARC) layer resting on the top. (b) A unit cell (Pitch P = 0.8 μm) consisting of a vertical waveguide with corresponding geometric parameters, directing the incident beam to Left/Right pixel based on its polarization state. (c) Design of pixel arrangement in the detector plane, consisting of Left (L), Right (R) pixels of size a = 0.56 μm.

Accepted Manuscript

To optimize the design parameters and analyse the performance matrix of the polarization splitter, numerical simulations were performed employing a finite difference time domain (FDTD) method. Initially, unit cell simulations were performed to optimize the structural parameters of the PS. The polarization splitter was excited with a broadband (400-700 nm) Gaussian beam with a 0.3 numerical aperture. Bloch boundary conditions were employed for X, Y directions, meanwhile perfectly matched layer (PML) boundary conditions were set for the propagation direction (z-axis). The refractive index of Si_3N_4 and SiO_2 were set as 2.04 and 1.46 [39]. For the final device, optimal device parameters were obtained by rigorous numerical optimizations, where the main figure of merit was set to maximize the power efficiency in the relevant active pixel, leading to a minimum power in the unwanted pixel, by optimizing lengths (H1 and H2) and top opening aperture (W1), while keeping the bottom aperture (W2) fixed at 200 nm to ensure a compact footprint. Finally, the best design with a maximum transmission efficiency in the designed pixel was chosen for the optimal device. The device measures 10.3 μm in total length with a 90 nm thick SiO_2 ARC. The 0.8 μm splitter pitch was chosen to be compatible with the smallest state-of-the-art CMOS imager of 0.56 μm pixel size [40].

Results and Discussion

The normalized electric-field intensity distribution profiles at plane C (Fig. 1b) for X and Y polarization states at three different wavelengths (448 nm, 538 nm, 640 nm) are shown in Figure 2a. The output waveguides area is highlighted by white squares in the field profiles. The polarization splitter directs the X-polarized incident beam to a tightly confined field spot in the left pixel (top-row), with a minimal intensity in the right pixel. Beating of the guided mode in the output waveguides results in a slightly shifted intensity peak position from the centre of the waveguide, as observed in the profile for 538 nm where the field spot lies in the bottom left corner of the output waveguide. Switching the input

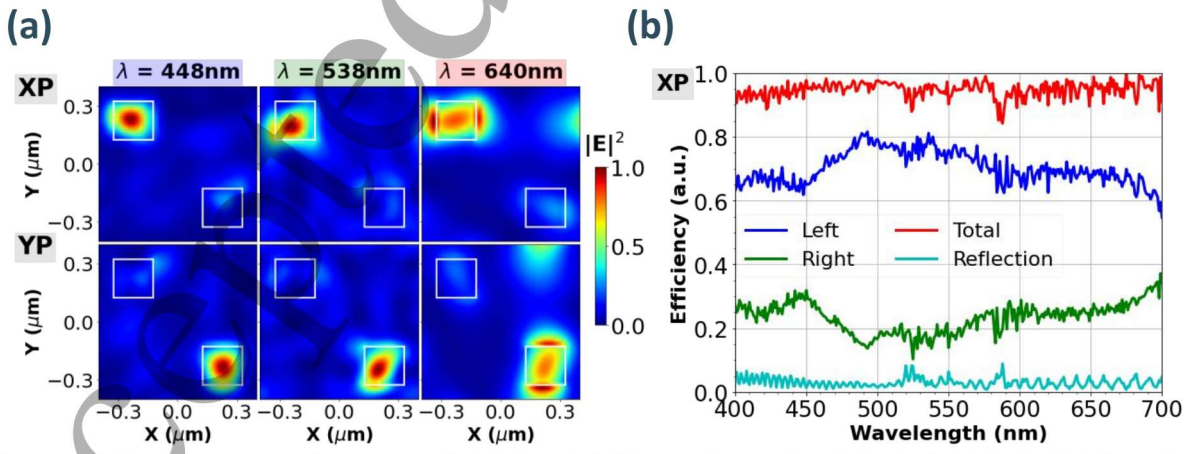

Figure 2. Performance of proposed device: (a) Normalized simulated electric-field intensity distribution profiles at the detector plane for two orthogonal polarization states at blue (448nm), green (538nm) and red (640nm) wavelengths. The device focuses the incident beam to left/right pixels for X/Y polarizations of incident beam over the whole visible spectrum. (b) Simulated transmission and reflection efficiency of the polarization splitter for X-polarized illumination within visible spectrum. Blue, green curves indicate the power transmitted to the left, right pixels, respectively. Red and cyan curves provide the total transmitted and reflected powers over the visible spectrum.

Accepted Manuscript

polarization from X to Y, results in transferring the beam to the right pixel with a maximum intensity (bottom row). Moreover, device performs similarly when excited with a plane wave (see supporting information S1), showing its potential to perform under different illumination conditions.

Transmission and reflection spectra for an X-polarized incident beam is given in Figure 2b. The PS is highly efficient with a near-unity total power transmission (averaged over full visible range), owing to a marginal reflection efficiency. The blue and green curves represent the amount of light detected in the left and right pixel, respectively. The left pixel detects more than 70% of the total power, whereas about 20% of the power is transmitted to its neighbour (right) pixel. A maximum polarization extinction ratio (PER) of ≈ 4:1 is achieved around the central wavelength 550 nm. The PS successfully splits the incident light based on its polarization state and directs it to its respective pixel at sub-micron level, with near unity power transmission efficiencies. **Table 01** shows a comprehensive comparison of our device with the available state-of-the-art polarization filters/splitters based on traditional metallic wire-grid, liquid crystals, thin-films and metasurface platforms. The comparison highlights that vertical waveguides can offer superior performance in terms of operating bandwidth, transmission efficiency and reduced pixel pitch of 560 nm which matches with the currently smallest CMOS imager pixel size, enabling its seamless integration with state-of-the-art imaging technologies. The polarization extinction ratio (PER) of our device is relatively low, but similar to the wiregrid-based solutions reported previously which successfully employed low-PER systems in applications like high-frequency electric-field imaging and microchemistry systems for the polarimetric measurements of chiral solutions by developing tailored algorithms [41]-[43]. A similar approach can be implemented to our proposed polarization splitting device to extend its potential applications from polarimetric measurements to remote sensing, biomedical imaging and agri-food sectors.

Work type	λ_d (μm)	Pixel size (μm)	Efficiency (%)	PER
Wire-grid polarizer (Exp.) [18], [43]	0.633 / 0.4-0.7	20 / 2.5	46 / 63	2.03 / 85
LC polymer (Exp.) [21]	0.45	8	NA	40-336
Thin-film polarizer (Exp.) [23]	0.633	5	66	330
Metasurfaces (Exp.) [24] / [36]	0.85 / 0.45-0.65	2.4 / 40	60 / 80	6 / 10
Vertical-Waveguides (Sim.) [This work]	0.4-0.7	0.56	70	4

Table 1. A comparison of the state-of-the-art polarization filter/splitter and the proposed vertical waveguide based splitter.

To further analyse the polarization sorting performance of the proposed device, we changed the simulation strategy from a unit cell to an array of 3x3 devices as shown in Figure 3. The array simulations were performed to better understand the response of device including contributions from the neighbouring devices. The array was excited with a single Gaussian beam (NA = 0.3) at the centre of the array as depicted in Figure 3a. The shaded circular region spotlights the shape and size of the Gaussian beam, meanwhile an inset represents the top view of the polarization splitter inside the array. Perfectly matched layer (PML) boundary conditions were employed for all directions. Figure 3b gives the simulated spectral efficiencies for the normal incident light illumination. The total power efficiency is defined as the amount of light collected by all

Accepted Manuscript

the pixels in the detector plane. A total power of more than 70% was transmitted to the detector plane, meanwhile the rest of the light scatters and ended up being absorbed by the simulation region sidewalls due to PML boundary conditions. The majority of the transmitted power was directed to the left pixels intended to collect X-polarized light, while the right pixels recorded over 15% resulting in the pixel cross-talk. Here, cross-talk is defined as the ratio of power transmission in the unwanted pixel to the total incident light. The higher cross-talk in the $\lambda > 600nm$ region appears to be due to the large gaussian beam size, as compared to the pixel size, at these wavelengths.

Figure 3c illustrates a breakdown of the transmitted power into the central and neighbouring left/right pixels. In the spectral region $400 < \lambda < 600\,nm$, central left pixel received an average of >30% light with lower cross-talks as the guided mode was highly concentrated inside the output waveguides. An increase in the photon size for $\lambda > 600nm$, results in a spreading of power to the neighbouring pixels which record more power. Normalized electric-field intensity profiles (zoomed-in view, full array view is shown in supporting information Figure S2) at wavelengths of 448 nm, 538 nm, and 640 nm, are presented in Figure 3d. The electric-field spots were highly concentrated in the middle of central left pixels over the whole visible range, confirming the polarization sorting ability of the device for an array case.

To evaluate device performance under realistic illumination conditions for image sensors, we simulated a uniform illumination by incoherently combining results from Gaussian source simulations at different (4, 9) positions [44]. A detailed discussion about the uniform illumination simulation method is presented in supporting information S3. A comparison of the device performance (Figure 3e) shows that a single Gaussian beam is sufficient to analyse the performance of the single device in the array for the designated

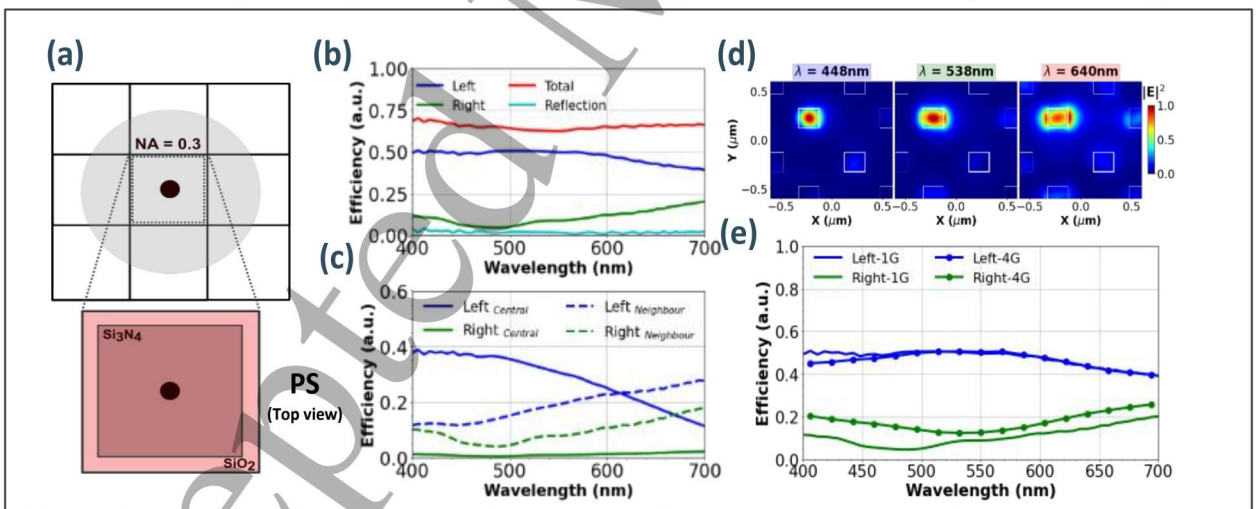

Figure 3. Demonstration of a 3x3 polarization splitter array response under single and multiple Gaussian excitation: (a) A schematic of the polarization splitter 3x3 array, with an inset of PS (top view). The array is excited with a single X-polarized Gaussian beam (NA=0.3) at the mid-point of central PS. (b) Simulated transmitted (red curve) and reflected power (cyan curve) as a function of wavelength. Power detected in the left, right pixels, obtained by integrating over array area, are shown by blue, green curves. (c) A comparison of power transmitted to the central (solid lines) and neighbouring (dashed lines) left/right pixels in the array. (d) Normalized electric-field intensity distribution profiles at three visible wavelengths: Blue (448 nm), Green (538 nm), and Red (640 nm). The white squares indicate the area of output waveguides uniformly distributed over the array. (e) A comparison of device spectral efficiency for single and four Gaussian (uniform illumination) excitations. The blue, green curves present the power transmitted to the left, right pixels for a single Gaussian (1G), and uniform illumination (4 Gaussian) conditions.

Accepted Manuscript

NA, hence reducing the simulation time by a factor of 4 (9) in comparison to the uniform illumination under 4 (9) Gaussian beams. From the detailed analysis discussed above, it is evident that the proposed device can efficiently collect most of the incoming light and sort the linear orthogonal X and Y polarization states with a maximum PER of 4:1 at central wavelength of 550 nm.

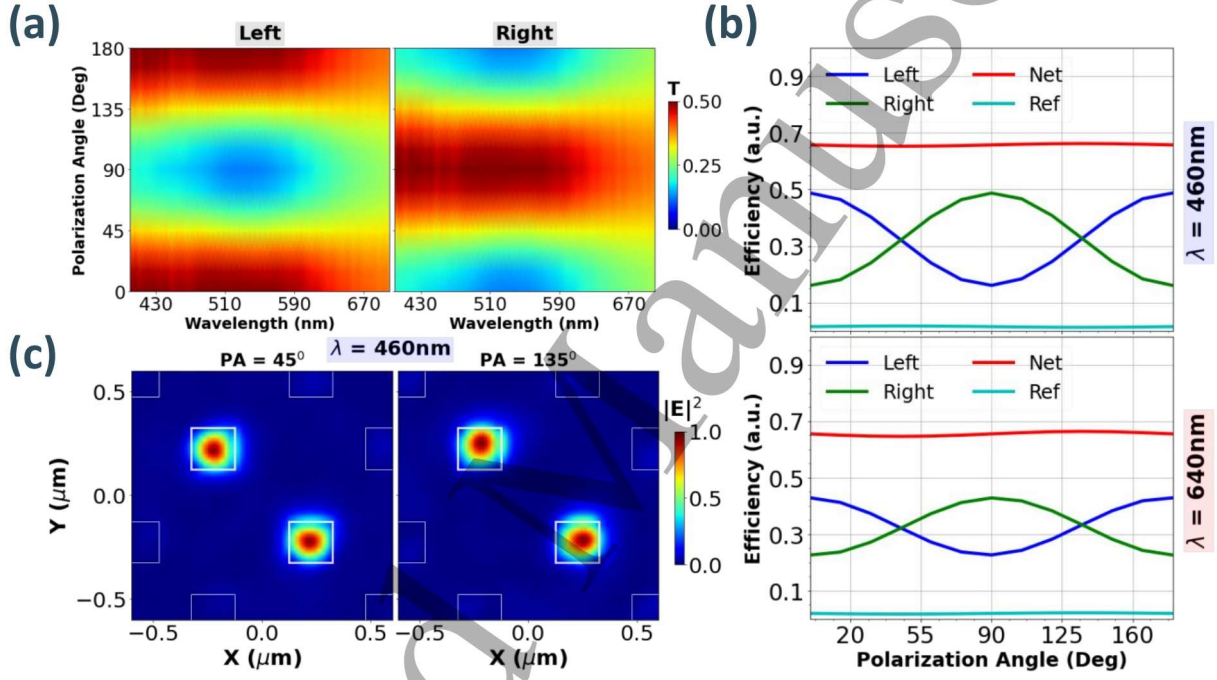

Figure 4. Polarization sorting capability of the device for full linear polarization space: (a) The simulated transmitted power for left and right pixels as a function of wavelength and polarization angle. (b) The flow of power from left to right pixels and vice versa for a change in the polarization angle at 460 nm and 640 nm, showing a good polarization sorting ability of the device over broadband visible spectrum. The red, cyan curves give the total transmitted and reflected power efficiencies. (c) Normalized electric-field intensity profiles for two cross polarization states (45º, 135º) at 460 nm.

To understand the device response under any arbitrary linear polarization state, simulations were performed by varying the polarization angle within a range of 0-180º, as shown in Figure 4. The simulated transmission spectra as a function of polarization angle across the visible spectrum for both left and right pixels are presented in Figure 4a. These transmission maps show a smooth transition of power from left to right, and vice versa as the polarization switches from one state to the other. The device performs well over the whole visible spectrum with a high routing efficiency ~50%, meanwhile a slightly higher cross-talk exists for the $\lambda > 650nm$ region, owing to the larger photon size. Figure 4b gives the simulated transmitted and reflected powers at 460 nm and 640 nm over the

Accepted Manuscript

polarization space. The total transmitted (red curve) and reflected (cyan curve) powers are found constant as 65% and 2% respectively, unaffected by a change in the polarization state of incident beam. The left pixel (blue curve) records a maximum power of >40% for the x-polarization, while <20% of the incident power goes to the right pixel. Power gradually shifts to the right pixel as the polarization is switched to the y-state. A similar behaviour is observed as the polarization angle is changed from 90º to 180º, but with mirror symmetry. For example, the cross-polarization states (45º and 135º) are indistinguishable, as both pixels share the same power at the intersecting points for blue and green curves. The normalized electric-field intensity profiles for cross-polarization states at 460 nm are depicted in the Figure 4c. The field spots are well confined within both output waveguides in the left and right pixel, and are identical for both polarization states. Finally, it is worth to mention that in addition to sorting the linear orthogonal (x, y) polarization states, the device can split any arbitrary linear polarization α in the range 0º-90º with different power ratios in Left/Right pixels, but records a similar power ratio to its counterpart $(180^{o} - \alpha)$ within 90º-180º owing to the geometrical symmetry of the proposed device.

We further extend the device capability to fully characterize the linear polarization state of light, hereto we not only need to split the x and y polarization states, but also the cross-polarization states to different pixels. This functionality was achieved by integrating a dielectric half-waveplate (HWP), sitting on the top of the polarization splitter. We designed a broadband (400-700 nm) HWP based on high index dielectric meta-atom arranged in a plus-shape configuration, with a compact pitch size of 400 nm (Figure 5a). More information on the HWP design is given in supporting information S4. The index of the HWP was chosen as n = 2.4, leaving design flexibility to employ TiO_2 or Nb_2O_5 for the final device realization. The 600 nm tall HWP is composed of two orthogonal rectangular nanofins with dimensions 100nm x 350nm and 150nm x 60nm. Figure 5b depicts a schematic of the 1.6µm x 0.8µm PS supercell design, which is composed of 4 pixels, two polarization splitters and a top layer of HWPs with different orientation angles i.e. 0º and 22.5º. By HWP definition, the PS with θ=0º HWP is responsible to mirror the polarization state $(\theta_p \rightarrow -\theta_p)$ of the incoming light around the y-axis, effectively mapping the x and y polarization on itself. Meanwhile the PS with θ=22.5º HWP mirrors around the 22.5º axis $(\theta_p \rightarrow 45^{o} - \theta_p)$, thus mapping the cross-polarization states 45º and 135º effectively on the x and y polarization respectively, allowing one the use the identical PS. A possible pixel design, which consists of 2 left and 2 right pixels with the corresponding labels, is shown in Figure 5c.

We analysed the device performance for an array of 3 x 3 HWPs integrated PS under uniform illumination for two Gaussian beams (X-polarized), a sketch is presented in Figure 5d. Figure 5e shows the simulated spectral response of the device array. Power in the left and right pixels were calculated by integrating over all L0, L22 and R0, R22 pixels respectively, meanwhile total and reflected powers indicate the total transmitted and reflected power in the full array area. Due to the HWP imperfect response over the whole visible spectrum, especially in the region $\lambda < 550nm$, the device efficiency slightly degrades with a total efficiency slightly below 50% for short wavelength as indicated by red curve. L0 is the main contributing pixel with an efficiency of around 20% and responsible for detecting the X-polarized incident beam. Pixels L0 and R0 respond quite similarly to the PS without HWPs and allows to distinguish orthogonal linear polarization

Accepted Manuscript

states (X, Y), whereas L22 and R22 pixels records a similar power as the 22.5º HWP converts the X-polarization in a cross-polarization illumination.

.

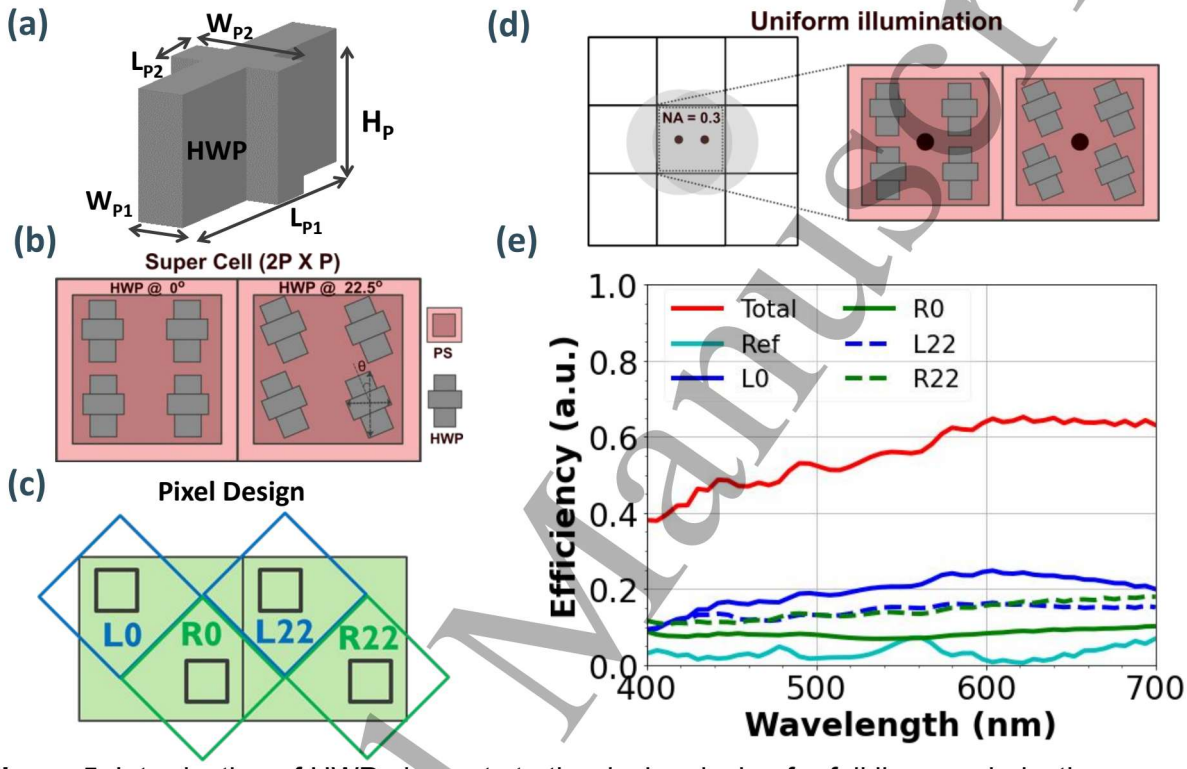

Figure 5. Introduction of HWP elements to the device design for full linear polarization space routing: (a) A schematic of the HWP design, which is a high index nanopost with a plus-shape cross section. (b) A sketch of the supercell with pitch 1.6μm x 0.8μm, composed of two polarization splitters with a top HWP layer. The HWPs are distributed periodically over unit cell with different orientation angles (θ = 0º, 22.5º). (c) Pixel configuration for the super cell consisting of four pixels. L0, R0 and L22, R22 correspond to the left, right pixels for PS with HWP orientated at 0º and 22.5º. (d) A schematic of the 3x3 supercell array for uniform illumination under 2 Gaussian beams. (e) Simulated transmitted and reflected power under X-polarized uniform illumination. A breakdown of total power transmitted to L0, L22 pixels (solid, dashed blue curves) and R0, R22 pixels (solid, dashed green curves), respectively.

Figure 6 shows the polarization splitting performance of the final device, the HWP integrated PS, over the full polarization space. The simulated transmission efficiencies for the left and right pixels as a function of polarization angle over the visible spectrum are presented in Figure 6a. Here, transmission efficiency in L0 represents the total amount of light collected in all the L0 pixels over the array, and similarly for R0, L22, and R22 pixels. These power transmission maps indicate a gradual shift of the maximum intensity from one pixel to the other as the polarization angle changes between 0-180º over the broad operational bandwidth of 400-700 nm. It can be observed that L0, R0 pixels record maximum power (~15-25%) for orthogonal x, y polarization states,

Accepted Manuscript

meanwhile cross-polarization states (45º, 135º) end up in the L22, R22 pixels with similar routing efficiencies of (~20-25%). Normalized electric-field intensity profiles for four different polarization states at 550 nm are shown in Figure 6b. A unique field distribution pattern exists for each polarization state, with maximum field intensity in the corresponding pixel. All four pixels gets a maximum efficiency for its designed polarization state as depicted in Figure 6c. However, R0 detects the corresponding polarization (Y) with a lower efficiency as compared to the other pixels, which could be attributed to the asymmetric response of the HWP for orthogonal polarization states. Finally, we conclude that the integration of additional HWP elements into the proposed PS, incident light beam with different linear polarizations can be successfully routed the to the relevant pixels across the visible spectrum. Nevertheless, it is worthy to mention that the device's functionality can be further extended to split the circular/elliptical polarizations by replacing the HWP with quarter-waveplate (QWP) elements orientated at an angle $\theta = \pm 45^{o}$ / $\theta \neq \pm 45^{o}$, respectively.

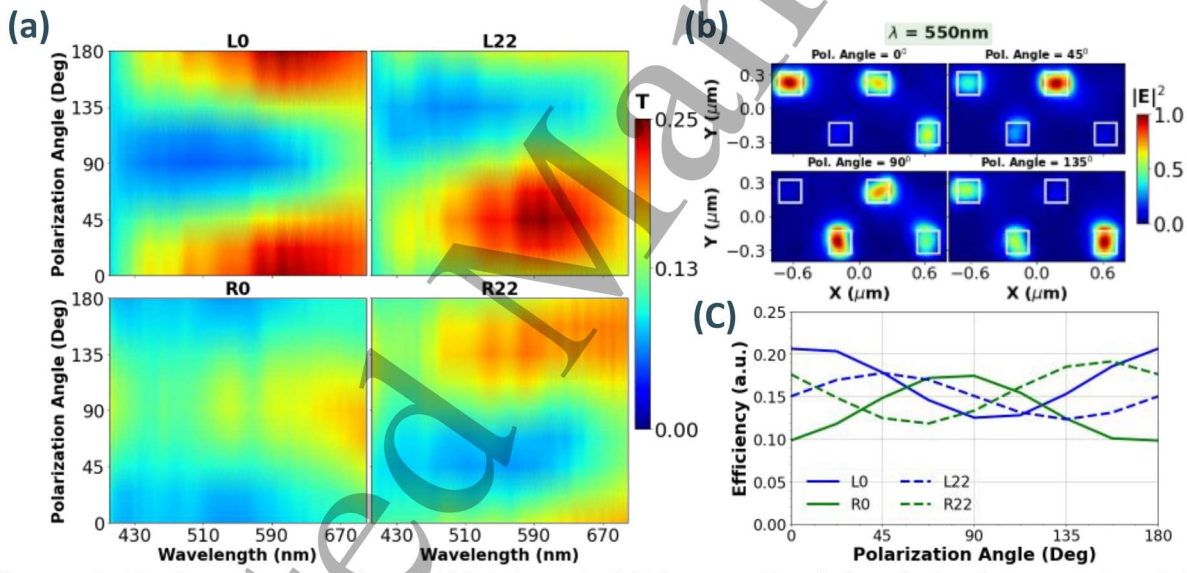

Figure 6. Performance of the HWP integrated PS over the full polarization spectra. (a) Simulated transmission efficiency, integrated over left/right pixels of the supercell array, as a function of polarization angle across the visible spectrum. The L0 and R0 pixels below the PS with HWP oriented at 0º record the maximum power for the orthogonal polarization states (x, y), whereas pixels L22, R22 which lie below the PS with HWP oriented at 22.5º receive the maximum power for the cross-polarization states (45º, 135º). (b) Normalized electric-field intensity pattern for the supercell array (cropped for a single supercell) in the detector plane for four different polarization states (X or 0º, Y or 90º, 45º, and 135º) at 550nm. The device routes and focus the input 0º, 90º, 45º, and 135º polarization states to field hotspots in the L0,

Finally, as the proposed device has shown promising simulation results, the next step is to fabricate the designed splitters for experimental verification to confirm the real efficiency of the system. We will employ our well-established vertical waveguide technology, which has already successfully demonstrated the color splitting functionality at sub-micron spatial resolution utilizing standard backend processing techniques on 300

Accepted Manuscript

mm wafers as briefly discussed in our previous work, to fabricate next-generation of vertical waveguides as proposed in this work [45]. Nonetheless, we foresee possible fabrication challenges due to high aspect ratio and non-uniform etch profiles along the propagation direction of the proposed structures. To address these concerns, we intend to slightly modify the fabrication recipe to develop the splitters in multiple layers (see supporting information S5) to ensure optimal etch-aspect-ratio and stress compensation without any structural collapse. Ultimately, the fabricated splitters will be optically characterized to validate their performance, paving the way for the development of sub-micron pixel sized polarization splitters with potential applications in high-resolution polarization imaging.

Conclusion

In conclusion, we have designed and simulated an ultracompact polarization splitter based on a vertical dielectric waveguide, demonstrating efficient collection and separation of linear polarization states across the visible spectrum (400-700 nm). The device successfully realizes polarization splitting with sub-micron pixel resolution (560 nm), matching with the pixel size of cutting-edge CMOS imagers. A comprehensive analysis reveals near-unity transmission efficiency with a polarization extinction ratio of 4:1 at central wavelength (550 nm). Additionally, integration of a half-wave plate element facilitates routing of the entire linear polarization band (0^o-180^o) to the designated pixels. Nonetheless, there is still room to further improve the device performance through advanced optimization methods and the use of high-index materials. As a future research direction, the device would be fabricated using advanced thin film deposition and lithography techniques, enabling the exploration of its full potential. We believe that this work lays the foundation for a new paradigm in imaging technology, offering a promising solution for high-resolution polarization imaging applications in polarimetric measurements, remote sensing, navigation and biomedical imaging.

Acknowledgement: We acknowledge the financial support from the Fund for Scientific Research Flanders (FWO) under Project number S004322N (GigaPixel).

Supporting information: Simulation data for plane wave excitation; Electric-field intensity distribution profiles for polarization splitter array for a Gaussian illumination; A detailed simulation method and results for uniform illumination; Half-waveplate design mechanism and simulated performance.

Conflict of interest: Authors state no conflicts of interest.

References:

[1] J. S. Tyo, D. L. Goldstein, D. B. Chenault, and J. A. Shaw, “Review of passive imaging polarimetry for remote sensing applications,” *Appl. Opt.*, vol. 45, no. 22, pp. 5453–5469, Aug. 2006, doi: 10.1364/AO.45.005453.

Accepted Manuscript

[2] N. M. Garcia, I. de Erausquin, C. Edmiston, and V. Gruev, “Surface normal reconstruction using circularly polarized light,” *Opt. Express*, vol. 23, no. 11, pp. 14391–14406, Jun. 2015, doi: 10.1364/OE.23.014391.
[3] S. Shwartz, E. Namer, and Y. Y. Schechner, “Blind Haze Separation,” in *2006 IEEE Computer Society Conference on Computer Vision and Pattern Recognition (CVPR’06)*, Jun. 2006, pp. 1984–1991. doi: 10.1109/CVPR.2006.71.
[4] L. B. Wolff, T. A. Mancini, P. Pouliquen, and A. G. Andreou, “Liquid crystal polarization camera,” *IEEE Trans. Robot. Autom.*, vol. 13, no. 2, pp. 195–203, Apr. 1997, doi: 10.1109/70.563642.
[5] J. R. Kuhn, D. Potter, and B. Parise, “Imaging Polarimetric Observations of a New Circumstellar Disk System,” *Astrophys. J.*, vol. 553, no. 2, p. L189, May 2001, doi: 10.1086/320686.
[6] D. L. Coffeen, “Polarization and scattering characteristics in the atmospheres of Earth, Venus, and Jupiter,” *JOSA*, vol. 69, no. 8, pp. 1051–1064, Aug. 1979, doi: 10.1364/JOSA.69.001051.
[7] T. Charanya *et al.*, “Trimodal color-fluorescence-polarization endoscopy aided by a tumor selective molecular probe accurately detects flat lesions in colitis-associated cancer,” *J. Biomed. Opt.*, vol. 19, no. 12, p. 126002, Dec. 2014, doi: 10.1117/1.JBO.19.12.126002.
[8] J. Zuo *et al.*, “Chip-integrated metasurface full-Stokes polarimetric imaging sensor,” *Light Sci. Appl.*, vol. 12, no. 1, p. 218, Sep. 2023, doi: 10.1038/s41377-023-01260-w.
[9] G. Horváth, Ed., *Polarized Light and Polarization Vision in Animal Sciences*. Berlin, Heidelberg: Springer, 2014. doi: 10.1007/978-3-642-54718-8.
[10] G. Kriska, B. Bernáth, R. Farkas, and G. Horváth, “Degrees of polarization of reflected light eliciting polarotaxis in dragonflies (Odonata), mayflies (Ephemeroptera) and tabanid flies (Tabanidae),” *J. Insect Physiol.*, vol. 55, no. 12, pp. 1167–1173, Dec. 2009, doi: 10.1016/j.jinsphys.2009.08.013.
[11] I. M. Daly *et al.*, “Dynamic polarization vision in mantis shrimps,” *Nat. Commun.*, vol. 7, no. 1, p. 12140, Jul. 2016, doi: 10.1038/ncomms12140.
[12] R. P. O’Shea, G. P. Misson, and S. E. Temple, “Seeing polarization of light with the naked eye,” *Curr. Biol.*, vol. 31, no. 4, pp. R178–R179, Feb. 2021, doi: 10.1016/j.cub.2020.12.037.
[13] A. Le Floch, G. Ropars, J. Enoch, and V. Lakshminarayanan, “The polarization sense in human vision,” *Vision Res.*, vol. 50, no. 20, pp. 2048–2054, Sep. 2010, doi: 10.1016/j.visres.2010.07.007.
[14] N. A. Rubin, G. D’Aversa, P. Chevalier, Z. Shi, W. T. Chen, and F. Capasso, “Matrix Fourier optics enables a compact full-Stokes polarization camera,” *Science*, vol. 365, no. 6448, p. eaax1839, Jul. 2019, doi: 10.1126/science.aax1839.
[15] A. G. Andreou and Z. K. Kalayjian, “Polarization imaging: principles and integrated polarimeters,” *IEEE Sens. J.*, vol. 2, no. 6, pp. 566–576, Dec. 2002, doi: 10.1109/JSEN.2003.807946.
[16] T. York and V. Gruev, “Characterization of a visible spectrum division-of-focal-plane polarimeter,” *Appl. Opt.*, vol. 51, no. 22, pp. 5392–5400, Aug. 2012, doi: 10.1364/AO.51.005392.
[17] S. Gao and V. Gruev, “Gradient-based interpolation method for division-of-focal-plane polarimeters,” *Opt. Express*, vol. 21, no. 1, pp. 1137–1151, Jan. 2013, doi: 10.1364/OE.21.001137.
[18] T. Yamazaki *et al.*, “Four-directional pixel-wise polarization CMOS image sensor using air-gap wire grid on 2.5-μm back-illuminated pixels,” in *2016 IEEE International Electron Devices Meeting (IEDM)*, Dec. 2016, p. 8.7.1-8.7.4. doi: 10.1109/IEDM.2016.7838378.
[19] L. B. Wolff, “Polarization camera for computer vision with a beam splitter,” *JOSA A*, vol. 11, no. 11, pp. 2935–2945, Nov. 1994, doi: 10.1364/JOSAA.11.002935.

Accepted Manuscript

[20] V. Gruev, R. Perkins, and T. York, "CCD polarization imaging sensor with aluminum nanowire optical filters," *Opt. Express*, vol. 18, no. 18, pp. 19087–19094, Aug. 2010, doi: 10.1364/OE.18.019087.
[21] Y. Wu *et al.*, "Flexible high-resolution thin micropolarizers for imaging polarimetry," *Chin. Opt. Lett.*, vol. 21, no. 3, p. 031301, Mar. 2023.
[22] J. Guo and D. Brady, "Fabrication of thin-film micropolarizer arrays for visible imaging polarimetry," *Appl. Opt.*, vol. 39, no. 10, pp. 1486–1492, Apr. 2000, doi: 10.1364/AO.39.001486.
[23] V. Gruev, A. Ortu, N. Lazarus, J. V. der Spiegel, and N. Engheta, "Fabrication of a dual-tier thin film micropolarization array," *Opt. Express*, vol. 15, no. 8, pp. 4994–5007, Apr. 2007, doi: 10.1364/OE.15.004994.
[24] E. Arbabi, S. M. Kamali, A. Arbabi, and A. Faraon, "Full-Stokes Imaging Polarimetry Using Dielectric Metasurfaces," *ACS Photonics*, vol. 5, no. 8, pp. 3132–3140, Aug. 2018, doi: 10.1021/acsphotonics.8b00362.
[25] A. V. Kildishev, A. Boltasseva, and V. M. Shalaev, "Planar Photonics with Metasurfaces," *Science*, vol. 339, no. 6125, p. 1232009, Mar. 2013, doi: 10.1126/science.1232009.
[26] D. Lin, P. Fan, E. Hasman, and M. L. Brongersma, "Dielectric gradient metasurface optical elements," *Science*, vol. 345, no. 6194, pp. 298–302, Jul. 2014, doi: 10.1126/science.1253213.
[27] A. Arbabi, Y. Horie, M. Bagheri, and A. Faraon, "Dielectric metasurfaces for complete control of phase and polarization with subwavelength spatial resolution and high transmission," *Nat. Nanotechnol.*, vol. 10, no. 11, pp. 937–943, Nov. 2015, doi: 10.1038/nnano.2015.186.
[28] M. Miyata, M. Nakajima, and T. Hashimoto, "High-Sensitivity Color Imaging Using Pixel-Scale Color Splitters Based on Dielectric Metasurfaces," *ACS Photonics*, vol. 6, no. 6, pp. 1442–1450, Jun. 2019, doi: 10.1021/acsphotonics.9b00042.
[29] M. Khorasaninejad *et al.*, "Polarization-Insensitive Metalenses at Visible Wavelengths," *Nano Lett.*, vol. 16, no. 11, pp. 7229–7234, Nov. 2016, doi: 10.1021/acs.nanolett.6b03626.
[30] W. T. Chen *et al.*, "Integrated plasmonic metasurfaces for spectropolarimetry," *Nanotechnology*, vol. 27, no. 22, p. 224002, Apr. 2016, doi: 10.1088/0957-4484/27/22/224002.
[31] A. Pors, M. G. Nielsen, and S. I. Bozhevolnyi, "Plasmonic metagratings for simultaneous determination of Stokes parameters," *Optica*, vol. 2, no. 8, pp. 716–723, Aug. 2015, doi: 10.1364/OPTICA.2.000716.
[32] M. Khorasaninejad, W. Zhu, and K. B. Crozier, "Efficient polarization beam splitter pixels based on a dielectric metasurface," *Optica*, vol. 2, no. 4, pp. 376–382, Apr. 2015, doi: 10.1364/OPTICA.2.000376.
[33] S. Liu, Z. Zhang, J. Cheng, X. Wang, S. Sun, and J. Xu, "Design of Full Stokes Vector Polarimetry Based on Metasurfaces for Wide-Angle Incident Light," *Photonics*, vol. 10, no. 4, Art. no. 4, Apr. 2023, doi: 10.3390/photonics10040382.
[34] Z. Guo *et al.*, "High-Efficiency Visible Transmitting Polarizations Devices Based on the GaN Metasurface," *Nanomaterials*, vol. 8, no. 5, Art. no. 5, May 2018, doi: 10.3390/nano8050333.
[35] Y. Zhang *et al.*, "Full Stokes Polarimetry for Wide-Angle Incident Light," *Phys. Status Solidi RRL – Rapid Res. Lett.*, vol. 14, no. 5, p. 2000044, 2020, doi: 10.1002/pssr.202000044.
[36] Y. Hu, Y. Jiang, Y. Zhang, Q. Wang, M. Pan, and H. Duan, "Achromatic Full Stokes Polarimetry Metasurface for Full-Color Polarization Imaging in the Visible Range," *Nano Lett.*, vol. 24, no. 41, pp. 13018–13026, Oct. 2024, doi: 10.1021/acs.nanolett.4c03785.
[37] J. Scott-Thomas, "Trends and Developments in State-of-the-Art CMOS Image Sensors," May 07, 2024. [Online]. Available: https://imagesensors.org/Past%20Workshops/2023%20Workshop/2023%20Papers/R11.pdf

Accepted Manuscript

[38] A. Nesic *et al.*, “Ultra-broadband polarisation beam splitters and rotators based on 3D-printed waveguides,” *Light Adv. Manuf.*, vol. 4, no. 3, pp. 251–262, Dec. 2023, doi: 10.37188/lam.2023.022.

[39] S. Nishiwaki, T. Nakamura, M. Hiramoto, T. Fujii, and M. Suzuki, “Efficient colour splitters for high-pixel-density image sensors,” *Nat. Photonics*, vol. 7, no. 3, pp. 240–246, Mar. 2013, doi: 10.1038/nphoton.2012.345.

[40] S. Park *et al.*, “A 64Mpixel CMOS Image Sensor with 0.56μm Unit Pixels Separated by Front Deep-Trench Isolation,” in *2022 IEEE International Solid- State Circuits Conference (ISSCC)*, San Francisco, CA, USA: IEEE, Feb. 2022, pp. 1–3. doi: 10.1109/ISSCC42614.2022.9731750.

[41] K. Sasagawa, R. Okada, M. Haruta, H. Takehara, H. Tashiro, and J. Ohta, “Polarization Image Sensor for Highly Sensitive Polarization Modulation Imaging Based on Stacked Polarizers,” *IEEE Trans. Electron Devices*, vol. 69, no. 6, pp. 2924–2931, Jun. 2022, doi: 10.1109/TED.2022.3140288.

[42] T. Tokuda, S. Sato, H. Yamada, and J. Ohta, “Polarization analyzing CMOS sensor for microchamber/microfluidic system based on image sensor technology,” in *2008 IEEE International Symposium on Circuits and Systems (ISCAS)*, May 2008, pp. 3162–3165. doi: 10.1109/ISCAS.2008.4542129.

[43] T. Tokuda, H. Yamada, K. Sasagawa, and J. Ohta, “Polarization-analyzing CMOS image sensor using monolithically embedded polarizer for microchemistry systems,” in *2009 IEEE International Symposium on Circuits and Systems*, May 2009, pp. 313–316. doi: 10.1109/ISCAS.2009.5117748.

[44] J. Vaillant, A. Crocherie, F. Hirigoyen, A. Cadien, and J. Pond, “Uniform illumination and rigorous electromagnetic simulations applied to CMOS image sensors,” *Opt. Express*, vol. 15, no. 9, pp. 5494–5503, Apr. 2007, doi: 10.1364/OE.15.005494.

[45] S. Kang *et al.*, “Wafer-level-integrated vertical-waveguide sub-diffraction-limited color splitters,” in *2023 International Electron Devices Meeting (IEDM)*, Dec. 2023, pp. 1–4. doi: 10.1109/IEDM45741.2023.10413746.

Accepted Manuscript